



Parameter extraction of gate tunneling current in metal–insulator–semiconductor capacitors based on ultra-thin atomic-layer deposited Al₂O₃

Hector Uribe-Vargas¹ · Joel Molina-Reyes¹

Received: 21 November 2017 / Accepted: 12 April 2018 / Published online: 18 April 2018
© Springer Science+Business Media, LLC, part of Springer Nature 2018

Abstract

Metal–insulator–semiconductor devices were fabricated using ultra-thin (6 nm) atomic layer deposited Al₂O₃. From I_g–V_g measurements, it was determined that the main conduction mechanisms for these devices are Ohmic conduction at very low electric fields ($E < 2 \text{ MV cm}^{-1}$) followed by Poole–Frenkel emission at medium electric fields ($E > 2 \text{ MV cm}^{-1}$) and finally, just before breakdown, Fowler–Nordheim ($E > 5 \text{ MV cm}^{-1}$). From the accurate verification of these conduction mechanisms, physical parameters such as barrier height (Φ_B), effective mass (m^*) and energy trap level (Φ_T) are extracted and could be used to effectively understand the performance and reliability of these devices under different substrate injection conditions.

1 Introduction

Understanding conduction mechanisms (CMs) through a thin dielectric oxide is important in state-of-the-art complementary metal–oxide–semiconductor (CMOS) technology. This is because when an electric field (E) is applied across the dielectric film, an undesired current appears which degrades the behavior of the device, thus shortening its life-span.

One of the most widely used dielectric in microelectronics is aluminum oxide (Al₂O₃) because it presents a large bandgap (~8.8 eV) and relatively high dielectric constant ($k \sim 9$); it also presents great thermal stability and can passivate interfaces enhancing the performance of devices [1–3].

This work reviews the conduction mechanisms in metal–insulator–semiconductor (MIS) devices using ultra-thin Al₂O₃ (6 nm in thickness) as gate oxide deposited by atomic-layer deposition (ALD). After gate patterning, MIS devices were electrically characterized using standard current–voltage (I_g–V_g), capacitance–voltage (C–V) and current–voltage–temperature (I_g–V_g–T) measurements, taking the devices to dielectric breakdown; afterwards,

experimental measurements were compared with semi-empirical tunneling models like Ohmic conduction (OC), Poole–Frenkel emission (PF) and Fowler–Nordheim tunneling (FN).

2 Experimental details

300 μm thick, n-type, 2–5 Ω cm resistivity, with a (100) surface plane silicon wafers were used as semiconductor substrate. Initial cleaning (RCA cleaning, HF-last) of these wafers was followed by thermal ALD of Al₂O₃ (6 nm in thickness) at 250 °C using trimethyl aluminum and water as precursors. Right after deposition of Al₂O₃, electron-beam evaporation of the metal gate (Aluminum = 400 nm at 10 Å s^{-1}) was done in ultra-high vacuum conditions while keeping a transitioning time (from ALD to evaporation) less than 2 min in order to minimize any exposure of Al₂O₃ to the clean room's atmosphere. Standard photolithography for wet-etching of aluminum was used in order to properly define the metal gate patterns. Figure 1a, b show the process flow and the fabricated MIS device. Figure 1c shows a scanning electron microscopy (SEM) image of the measured devices.

After fabrication, the devices were characterized using a semiconductor-device analyzer (SDA 4200 from Keithley), and at least 15 devices were measured in order to ensure reproducibility. I_g–V_g, C–V, and I_g–V_g–T measurements

✉ Hector Uribe-Vargas
hecuribe@inaoep.mx

¹ Electronics Department, National Institute of Astrophysics, Optics and Electronics, Luis Enrique Erro No. 1, Santa Maria Tonantzintla, Puebla C.P. 72840, Mexico

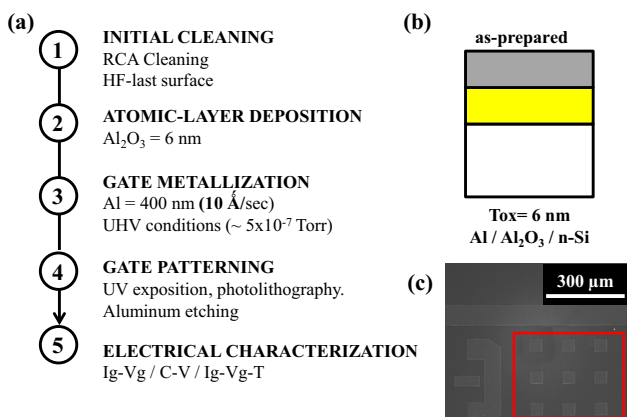


Fig. 1 **a** Process flow for fabrication of MIS structures using Al_2O_3 as gate oxide, **b** schematic of the resulting MIS structure having $T_{\text{ox}} = 6 \text{ nm}$. **c** Scanning electron microscopy (SEM) image of devices measured (gate area $60 \mu\text{m} \times 60 \mu\text{m}$)

were made at room temperature, in dark conditions, and with electromagnetic isolation.

3 Results and discussion

Figure 2a shows the $I_g\text{-}V_g$ experimental data for the fabricated MIS devices having $\text{Al}_2\text{O}_3 = 6 \text{ nm}$. As seen, all devices measured present the same $I_g\text{-}V_g$ characteristics, which is a direct result of the high quality in the ALD technique, where there is a total control in thickness and stoichiometry

of Al_2O_3 thus resulting in a high uniformity regarding the electrical reproducibility of these devices. After normalization to area and oxide thickness, current density–electric field (J–E) experimental data is shown in Fig. 2b. From these curves, at least three distinctive slopes are identified, which could be associated to different conduction mechanisms. As seen in Fig. 2b, an average electric field to breakdown of 7 MV cm^{-1} (4.3 V) is obtained, which is an excellent value for this oxide [4, 5]. After the dielectric breakdown occurs, the device could no longer be used as an effective insulator, as seen by the higher leakage current obtained in the return path (Fig. 2a, b).

By using the first derivative of gate current with respect to gate voltage (dI_g/dV_g), we are able to estimate the energy bandgap for Al_2O_3 during $I_g\text{-}V_g$ measurements (Fig. 3). We found $E_g (\text{Al}_2\text{O}_3)$ to be close to eight. These values are in agreement with the reported amorphous bulk material band-gap values of Al_2O_3 [6, 7].

Figure 4 shows the C–V characteristics for the MIS devices; from these measurements a $k \sim 5.72$ was obtained, which is below the expected value of $k \sim 9$ [4, 5, 8], this low value is due to the formation of an interface layer (IL) between $\text{Al}_2\text{O}_3/\text{Si}$, this IL is usually an aluminosilicate (AlSi_xO_y) which lowers the overall dielectric constant of the ultra-thin film. The flat band voltage (V_{fb}) is extracted considering an initial measurement from inversion to accumulation and the obtained value is -0.67 V . This reduction in the ideal value of V_{fb} (0 V) for the $\text{Al}/\text{Al}_2\text{O}_3/\text{n-Si}$ structure is due to a poor quality at the interface between $\text{Al}_2\text{O}_3/\text{Si}$, given by a density of interfacial

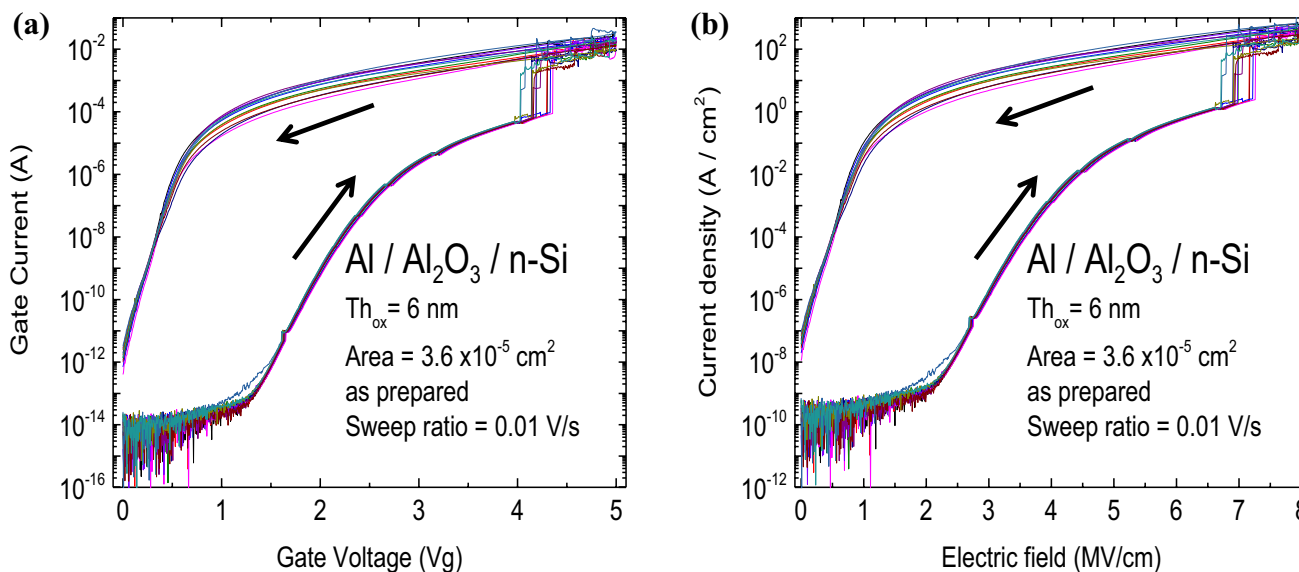


Fig. 2 **a** $I_g\text{-}V_g$ characteristics for MIS devices using ultra-thin Al_2O_3 as gate oxide with $t_{\text{ox}} = 6 \text{ nm}$, **b** J–E characteristics of MIS devices, after normalizing the former $I_g\text{-}V_g$ data to device area and oxide

thickness respectively. At least 10–15 MIS devices were measured in order to ensure reproducibility

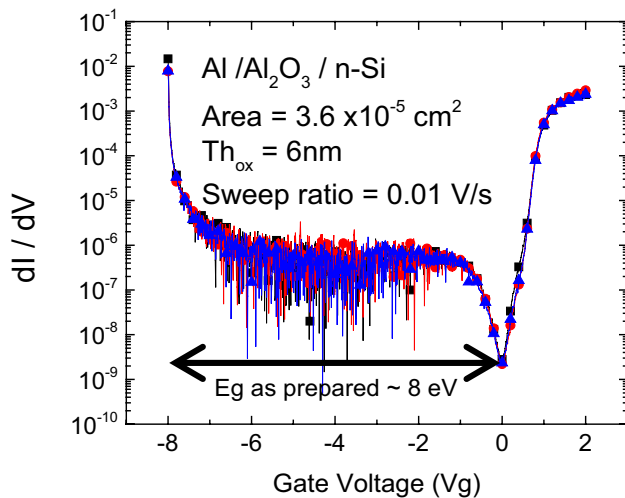


Fig. 3 The conductance method or first-derivative of gate current with respect to gate voltage (dI/dV_g) enables estimating the energy gap for Al_2O_3 -based MIS devices $E_g(\text{Al}_2\text{O}_3) \sim 8$

states (D_{it}) of $1.6 \times 10^{12} \text{ cm}^{-2} \text{ eV}^{-1}$ (typical value for $\text{SiO}_2/\text{Si} \sim 1 \times 10^{10} \text{ cm}^{-2} \text{ eV}^{-1}$ [9]). This high value of D_{it} creates positive charge at the $\text{Al}_2\text{O}_3/\text{Si}$ interface as seen in the inset of Fig. 4a, and it does so by enabling the filling and emptying of surface states with applied bias, which in turn, results in a negative shift of the complete C–V curve (reducing the flat band voltage [10–12]) while also producing a large hysteresis window. Additionally, Al_2O_3 has a high ratio of oxygen vacancies which are distributed through the bandgap, an oxygen vacancy with positive charge O^{2+} is located at

$\Phi_1 = 3.9 \text{ eV}$ above the valence band (VB) of Al_2O_3 [13–16], which coincides with the VB of Si resulting in the formation of dipoles near that interface and thus, contributing to Vfb reduction (oxygen vacancies with negative charge O^- would produce an energy trap level located at $\Phi_2 = 1.8 \text{ eV}$ below the conduction band of Al_2O_3 and are responsible for the Poole–Frenkel emission [16, 17]). Considering that the $\text{Al}_2\text{O}_3/\text{Si}$ system could develop a thin IL (AlSi_xO_y) in between, the difference in the oxygen density for bulk Al_2O_3 and the IL could also promote dipole formation at the $\text{Al}_2\text{O}_3/\text{IL}$ interface when charged oxygen vacancies migrate from the region of higher oxygen density towards the region of lower oxygen density [18–21]. When double sweep C–V measurements are performed, these devices present a hysteresis window of almost 1 V (Fig. 4a, b). This large hysteresis is associated mainly to the trapping-detrapping of charge via a large density of interface states D_{it} ; nevertheless, D_{it} could be drastically reduced by a passivation of the dangling bonds between insulator–semiconductor either by post metallization annealing [22, 23] or the growth of an interfacial SiO_x layer before deposition [24, 25], thus also influencing the final value of Vfb and hysteresis.

In order to correctly evaluate the conduction mechanism associated with the MIS device, and due to the fact that these are temperature-sensitive, I_g–V_g–T measurements (from 300 K up to 355 K) were performed. At low electric fields $E \leq 2 \text{ MV cm}^{-1}$, OC is the main conduction mechanism for these devices [17, 26, 27]; this mechanism is not temperature-dependent. When the electric field is increased ($E > 2 \text{ MV cm}^{-1}$), PF emission becomes the

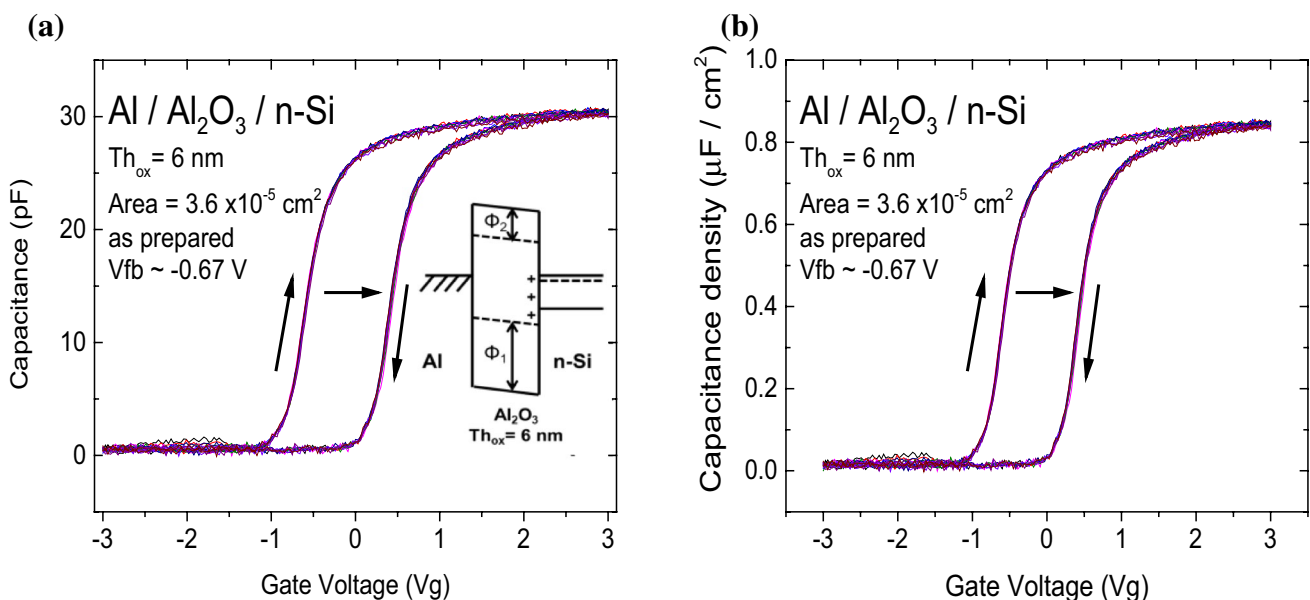


Fig. 4 **a** C–V characteristics of the MIS devices, the extracted dielectric constant is around 5.72, the large hysteresis is attributed to an overall high net negative charge, which produces the shift to the right in the flat band voltage, **b** normalized capacitance to area

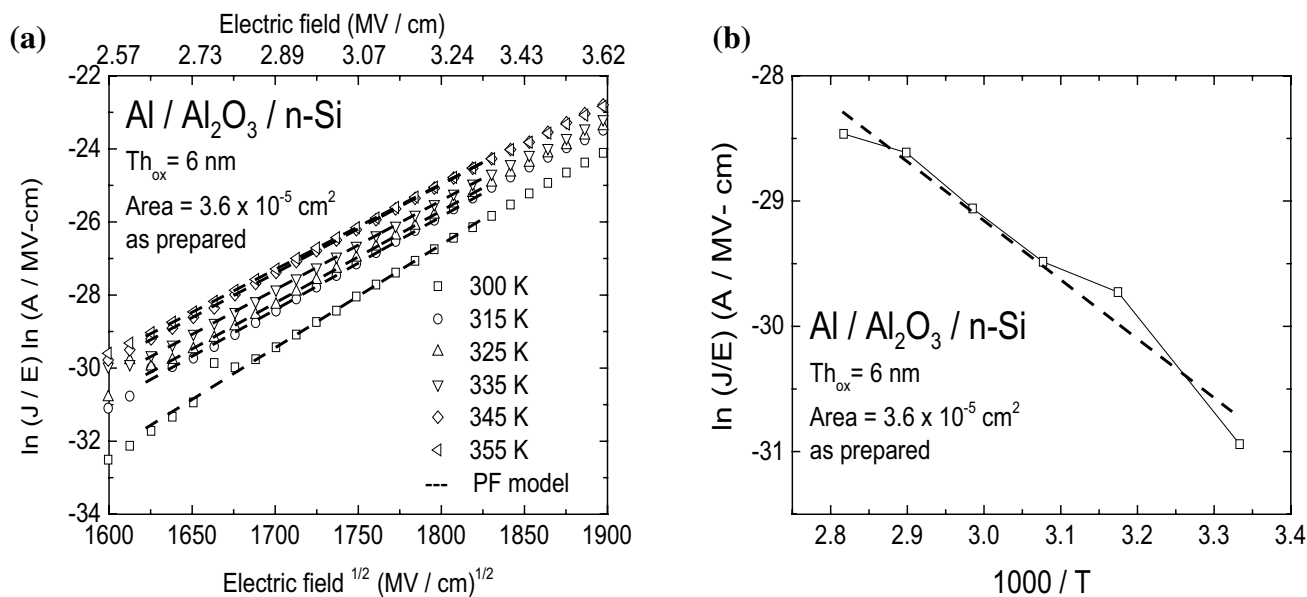


Fig. 5 a Fitting of the experimental J–E data to the Poole–Frenkel semiempirical model, b Arrhenius plot extracted from the Poole–Frenkel data

Table 1 Summary of the parameters extracted from experimental data, semi empirical models and simulations

Parameter	Al ₂ O ₃ (6 nm)
Dielectric constant (ϵ_r)	5.72
Effective mass [m^* ($m^* \times m_0$)]	0.4
Optical dielectric constant (ϵ_r)	1.47
Refractive index (η)	2.25
Energy trap level, Φ_T (eV)	1.53
Barrier height, Φ_B (eV)	1.7
Gate current density at $V_g = 1$ V, J_g ($A\text{ cm}^{-2}$)	2×10^{-10}
Electric field to breakdown, E_{bkd} ($MV\text{ cm}^{-1}$)	7
Flat band voltage, V_{fb} (V)	-0.67
Interface-states density, D_{it} ($\text{cm}^{-2}\text{ eV}^{-1}$)	1.6×10^{12}

main conduction mechanism, as seen in the fitting of the experimental data in Fig. 5.

From this fitting, energy trap level (Φ_T) and optical dielectric constant (ϵ_r) are extracted and shown in Table 1. The table shows an $\Phi_T \sim 1.53$ eV which means deep traps in the bandgap of the oxide. These values are consistent with defects associated to oxygen vacancies in a deep state at ~ 1.8 eV below the conduction band (CB) edge of the Al₂O₃ [13–16]. It was also determined that this type of defect corresponds to negative oxygen states, which would account for the transport and trapping properties in Al₂O₃. For $E > 4.5$ MV cm⁻¹, a pure PF mechanism no longer could be identified, so a combination of PF and FN appears. For even higher E (> 5 MV cm⁻¹), a pure FN

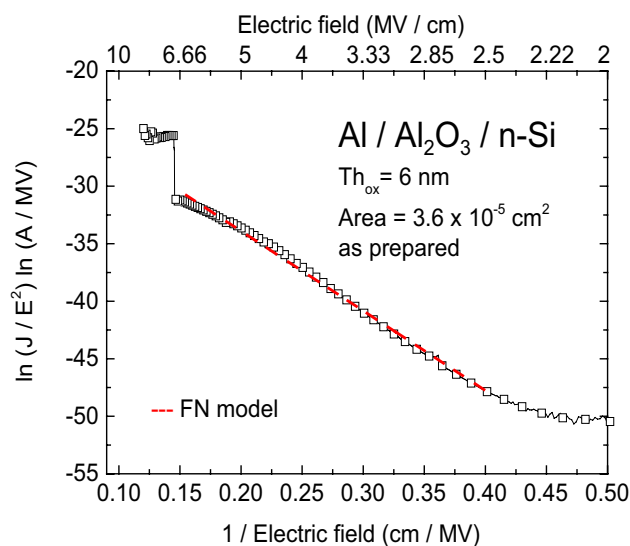


Fig. 6 Fitting of experimental I_g - V_g data of MIS devices (Al₂O₃=6 nm) to the Fowler–Nordheim conduction model. This conduction model appears at higher electric fields in all samples while lasting all the way up to dielectric breakdown

conduction mechanism is observed just before dielectric breakdown, as seen in Fig. 6.

Using the FN model, important physical parameters like barrier height (Φ_B) and effective mass (m^*) are extracted from fitting the model with experimental data, see Table 1. For these devices, a barrier height of $\Phi_B \sim 1.7$ eV and an effective mass of $0.4 m_0$ (where m_0 is the free electron mass) is obtained. All extracted parameters were compared to those

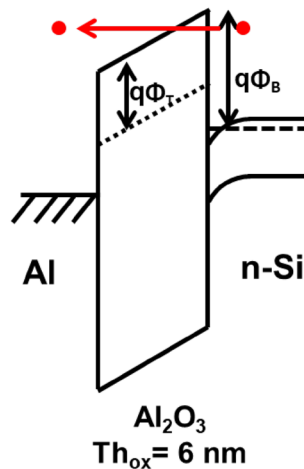


Fig. 7 Ideal band diagram for MIS devices, showing Φ_T and Φ_B as important parameters that will influence gate tunneling currents

found in literature, having excellent agreement [16, 17, 28, 29]. Table 1 below summarizes the main physical, electronic and performance parameters obtained from all the experimental data extracted from the fabricated MIS devices. By obtaining the physical parameters associated to the conduction mechanisms, predictions about the performance of these MIS devices fabricated with ALD ultra-thin Al₂O₃ could be made. For instance, increasing the barrier height Φ_B will result in an increased electric field to breakdown in the FN regime, also, pushing the energy trap level Φ_T towards the CB, will result in an increased leakage current when PF is the main conduction mechanism. Moreover, increasing the Al₂O₃ thickness in the fabricated devices will develop a larger Al_xSiO_y interface layer between Al₂O₃ and Si due to increased exposure to low pressure and temperature within the ALD chamber. In turn, this correlation between physical parameters and I_g-V_g characteristics results in the accurate determination of electrical properties of these MIS devices, and therefore its use for different applications.

Finally, Fig. 7 shows an accurate band diagram for all conduction mechanisms (substrate injection) for this oxide. As seen, if the barrier height Φ_B (associated with FN) is increased, the electron would need more energy to pass this barrier, thus resulting in increased electric field to breakdown. In the same way, if the energy trap level Φ_T moves deeper into the energy gap of Al₂O₃ (by defects associated to specific charged oxygen vacancies), leakage current would be reduced due to electrons needing more energy to go from this level to the conduction band of Al₂O₃ in the PF mechanism, and therefore, a lower dependence with temperature would be expected. In this respect, the position of Φ_T with respect to the conduction band in Al₂O₃ is quite relevant given that for some operation conditions, large current densities tunneling into Al₂O₃ would produce Joule heating [30,

31] and therefore, device degradation and its early failure should be properly predicted by reliability models that consider this correlation between Φ_T and temperature.

4 Summary and conclusions

In summary, current conduction mechanisms were identified in fabricated MIS devices having ultra-thin ALD Al₂O₃ (6 nm in oxide thickness) as gate oxide. From the fitting of semi-empirical current conduction models with experimental data, it was determined that for lower electric fields ($E < 2 \text{ MV cm}^{-1}$) the main conduction mechanism is Ohmic conduction followed by Poole–Frenkel emission at intermediate electric fields ($E > 2 \text{ MV cm}^{-1}$), and finally, Fowler–Nordheim tunneling just before breakdown ($E > 5 \text{ MV cm}^{-1}$). From the extraction of physical parameters associated to each conduction mechanism, a simple but practical correlation of materials' properties with device performance could be obtained. For instance, oxides with increased barrier heights Φ_B (same thickness) would result in larger electric field to breakdown; similarly, oxides whose energy trap level Φ_T gets closer to its conduction band, would result in higher leakage currents due to a higher temperature dependence. Given that the I–V and C–V characteristics for these MIS devices are highly dependent on the quality of Al₂O₃ and its interface with silicon, the presence of defects like oxygen vacancies or interface states, will also have a major impact on the performance of these simple devices. Therefore, a simple mechanism explaining conduction models correlated to energy trap levels given by these defects (present in Al₂O₃ and at its interface with silicon), help us to understand and possibly modulate, the electrical behavior of these devices. Finally, the high reproducibility, conformality, outstanding control (to atomic level) on the thickness and stoichiometry, interface properties with the semiconductor substrate, and the low deposition temperature ($T \leq 250 \text{ }^\circ\text{C}$) for these metal oxides, puts atomic-layer deposition as a powerful deposition technique which enables enhanced performance and therefore, better reliability predictions for electron devices based on these oxides.

Acknowledgements This work was fully supported by the Mexican Council for Science and Technology (CONACYT-Mexico).

References

1. J.M. Reyes, B.M. Perez Ramos, C.Z. Islas, W.C. Arriaga, P.R. Quintero, A.T. Jacome, J. Electrochem. Soc. **160**, B201–B206 (2013)
2. G. Dingemans, W.M.M. Kessels, J. Vac. Sci. Technol. A **30**, 1–27 (2012)

3. G. He, Z. Sun, *High-k Gate Dielectrics for CMOS Technology* (Wiley, Hoboken, 2012)
4. J.W. McPherson, J. Kim, A. Shanware, H. Mogul, J. Rodriguez, *IEEE Trans. Electron. Dev.* **50**, 8 (2003)
5. M. Lorenz, M.S. Ramachandra Rao, T. Venkatesan, E. Fortunato, P. Barquinha, R. Branquinho, D. Salgueiro, R. Martins, E. Carlos, A. Liu, F.K. Shan, M. Grundmann, H. Boschker, J. Mukherjee, M. Priyadarshini, N. DasGupta, D.J. Rogers, F.H. Teherani, E.V. Sandana, P. Bove, K. Rietwyk, A. Zaban, A. Veziridis, A. Weidenkaff, M. Muralidhar, M. Murakami, S. Abel, J. Fompeyrine, J. Zuniga-Perez, R. Ramesh, N.A. Spaldin, S. Ostanin, V. Borisov, I. Mertig, V. Lazenka, G. Srinivasan, W. Prellier, M. Uchida, M. Kawasaki, R. Pentcheva, P. Gegenwart, F. Miletto Granozio, J. Fontcuberta, N. Pryds, *J. Phys. D* **49**, 433001 (2016)
6. E.O. Filatova, A.S. Konashuk, *J. Phys. Chem. C* **119**, 20755–20761 (2015)
7. D. Tahir, H.L. Kwon, H.C. Shin, S.K. Oh, H.J. Kang, S. Heo, J.G. Chung, J.C. Lee, S. Tougaard, *J. Phys. D* **43**, 255301 (2010)
8. A. Bouazra, S.A.-B. Nasrallah, M. Said, A. Poncet, *Res. Lett. Phys.* **2008**, 286546 (2008)
9. D.K. Schroder, *Semiconductor Material and Device Characterization* (Wiley, Hoboken, 2005)
10. Z. Xiao-Hu, H. An-Ping, X. Zhi-Song, Y. Zhi-Chao, W. Mei, P.K. Chu, Y. Xiao-Dong, *Chin. Phys. B* **20**(No. 9), 097303 (2011)
11. H.L. Chang, M.S. Liang, *Appl. Phys. Lett.* **97**, 041912 (2010)
12. N.P. Maity, R. Maity, R.K. Thapa, S. Baishya, *Adv. Mater. Sci. Eng.* **2014**, 497274 (2014)
13. D. Liu, J. Robertson, *Microelectron. Eng.* **86**, 1668–1671 (2009)
14. D. Liu, S.J. Clark, J. Robertson, *Appl. Phys. Lett.* **96**, 032905 (2010)
15. M. Choi, A. Janotti, C.G. Van de Walle, *J. Appl. Phys.* **113**, 044501 (2013)
16. H. J. Molina, Uribe, *Thin Solid Films* **638**, 48–56 (2017)
17. H. Spahr, S. Montzka, J. Reinker, F. Hirschberg, W. Kowalsky, H.H. Johannes, *J. Appl. Phys.* **114**, 183714 (2013)
18. K. Kita, A. Toriumi, *Appl. Phys. Lett.* **94**, 132902 (2009)
19. K. Iwamoto, Y. Kamimuta, A. Ogawa, Y. Watanabe, S. Migita, W. Mizubayashi, Y. Morita, M. Takahashi, H. Ota, T. Nabatame, A. Toriumi, *Appl. Phys. Lett.* **92**, 132907 (2008)
20. X. Wang, K. Han, W. Wang, S. Chen, X. Ma, D. Chen, J. Zhang, J. Du, Y. Xiong, A. Huang, *Appl. Phys. Lett.* **96**, 152907 (2010)
21. L.Q. Zhu, K. Kita, T. Nishimura, K. Nagashio, S.K. Wang, A. Toriumi, *Jpn. J. Appl. Phys.* **50**, 031502 (2011)
22. C. Chakraborty, *J. Adv. Dielectr.* **4**, 1450023 (2014)
23. N. A. Winzer, P.M. Szabó, Wachowiak, J. Jordan, T. Heitmann, Mikolajick, *J. Vac. Sci. Technol. B* **01A**, 106 (2015)
24. R. Kotipalli, R. Delamare, O. Poncelet, X. Tang, L.A. Francis, D. Flandre, *EPJ Photovolt.* **4**, 1–8 (2013)
25. M. Valla, A.J. Rossini, M. Caillot, P. Raybaud, M. Digne, A. Chaumonnot, A. Lesage, L. Emsley, J.A. Van Bokhoven, C. Copéret, *J. Am. Chem. Soc.* **137**(33), 10710–10719 (2015)
26. K.Y. Cheong, J.H. Moon, H.J. Kim, W. Bahng, N.-K. Kim, *Appl. Phys. Lett.* **90**, 162113 (2007)
27. S. Ganguly, J. Verma, G. Li, T. Zimmermann, H. Xing, D. Jena, in *69th Annual Device Research Conference, DRC* (2011), pp. 121–122
28. Y. Liu, S. Shen, L.J. Brillson, R.G. Gordon, *Appl. Phys. Lett.* **98**, 3–5 (2011)
29. M.L. Huang, Y.C. Chang, C.H. Chang, T.D. Lin, J. Kwo, T.B. Wu, M. Hong, *Appl. Phys. Lett.* **89**, 53–56 (2006)
30. S. Chatterjee, Y. Kuo, J. Lu, J.Y. Majhi, P. Tewg, *Microelectron. Reliab.* **46**, 69–76 (2006)
31. R. Ranjan, K.L. Pey, C.H. Tung, L.J. Tang, G. Groeseneken, L.K. Bera, S. De Gendt, *IEDM Conf.* (2004)